Screening of the Coulomb interaction in C₃N: Reduced dimensionality and electronic structure effects

M. Amiri, F. Bagherpour, and H. Hadipour

Department of Physics, University of Guilan, Rasht 41335-1914, Iran

Coulomb interactions in two-dimensional semimetals like graphene are not screened in the usual way, and sizable long-range interaction has been found. With the aim of achieving new materials with nonconventional screening, as well as, in order to investigate various effects such as reduced dimensionality and electronic band dispersion, we calculate the strength of the effective Coulomb interaction U between p_z electrons in recently developed hexagonal C₃N materials from the first principles using the constrained random-phase approximation. We find that the calculated parameters in the monolayer of the C₃N are larger than the ones in graphene and remain sizable even in metallic bilayers. Nonlocal Coulomb interactions $U(r)$ in nonmetallic C₃N nanoribbons are almost 1 eV smaller than the ones for C₃N monolayer. Our results show that similar to graphene, screening in hexagonal C₃N is also nonconventional. This controversial screening of Coulomb interaction stems from the electronic structure and massless Dirac dispersion below Fermi energy, which has to be preserved for symmetry reasons in hexagonal C₃N layers.

I. INTRODUCTION

Two-dimensional (2D) materials such as graphene have become the subject of intensive theoretical and experimental investigations in the last decade due to the Dirac-type band dispersion [1,2]. Despite the substantial interest, the gapless energy dispersion of graphene limits it to be used in practical digital circuits. Likely to graphene, the monolayer of the other members of the group IV elements, namely silicene [3], germanene [4], and stanene [5], are zero-band-gap semiconductors. Different standard approaches such as atom adsorption [6–9] and edge engineering [10] are developed to open the band gap in graphene. Unfortunately, these methods are not able to be precisely controlled for realistic applications. Also, chemical doping or turning of graphene into nanoribbon gives rise to significant structural distortions that changes electronic structure, thereby forcing graphene to lose most of its advantages. For example, when we use hydrogen absorption, the sublattice symmetry that protects the Dirac cones is broken. Therefore, they cannot be used to understand the properties related to the Dirac fermions, such as the field of topological quantum matter [11–13] or quantum gravity [14]. So, tracking new carbon-based Dirac materials with reasonable band gap is a long-standing goal.

One way to find new graphenelike materials is to maintain graphene's lattice and then see what happens by replacing C atoms with its neighboring elements in the periodic table. Recently, semiconducting behavior has been observed in graphenelike ordered carbon-nitrogen structure C₃N with a band gap of 0.39–1.2 eV [15–20]. It possesses the 2D honeycomb lattice with D_{6h} point group symmetries [15]. So, similar to graphene, the chiral symmetry stabilizes the Dirac nodes in C₃N, with the difference that substitution of N atoms

shift the Fermi level from that of graphene and open a band gap.

Furthermore, hydrogenation and production of nanoscale systems provide a novel way to tune the properties of C₃N with unknown potential for applications. The band gaps of 1.8–5.5 nm-size quantum dots were found to be in the range 2.74 to 1.57 eV [15]. So, C₃N is considered to be promising materials field-effect transistors due to their appropriate band gap. The other important applications are the use of such systems in thermoelectric and anode material development [21,22]. Moreover, Cutting C₃N along with particular directions, which produce C₃N nanoribbons with armchair and zigzag edges, gives rise to the large band gap of 2–3 eV [23]. In the case of C₃N nanoribbons, ribbon width, thickness, and functionalizing of the ribbons' edge can thus lead to significantly affecting the electronic properties of the nanoribbons. Also, electronic and optical properties of C₃N maybe drastically modified by the adsorption of atoms like hydrogen on the C₃N surface [24]. For example, the fully hydrogenated C₃N is an insulator with a large band gap of about 2.8–4.1 eV [24].

The discovery of 2D materials is important not only in their application in industry, they can also increase our fundamental understanding of underlying physics of low-dimensional systems. In graphene, in spite of semimetallic behavior, the screening is weak, and a comparatively large $U/t \sim 3.5$ was obtained [8,25,26], where t is the nearest-neighbor hopping parameter. However, rather large nonlocal Coulomb interaction around 4.1 eV [26] and sizable bandwidth compared to other well-known 2D systems such as transition metal dichalcogenides [27], transition metal halides [28–30], and *MX*-enes [31,32], indicates that the gradient of Coulomb interaction is small and put graphene in the weakly correlated regime. Due to the nonconventional screening, for systems

with Dirac dispersion nonlocal Coulomb interactions make the phase diagram of hexagonal lattice more complicated and put the system in close proximity to both a spin-density wave and a charge density wave transition line [25]. Although it is questionable that the root of this nonconventional screening of graphene is related to the presence of a Dirac cone or not.

Furthermore, theoretical studies for a system with linear dispersion indicate that at small momentum transfer q polarization function is almost constant and in $q > 2k_F$ the static screening increases linearly with q [25,33]. This is completely different from what happens in a normal 2D system with quadratic bands where the polarization function decreases sharply with increasing q with a peak around $q = 2k_F$ [34]. This screening behavior of a system with a linear dispersion like graphene is typical of an insulator. These works emphasize that this strange screening can be traced back to the zero-gap chiral relativistic nature of graphene. It means that from the point of view of screening, electrons in linear bands behave like electrons in an insulator and do not screen well long-range Coulomb interactions. Furthermore, for graphene, Wehling *et al.* indicated that cRPA calculations give $\epsilon = 2.4$ for intermediate momentum q, and $\epsilon = 1$ for $q = 0$ which confirm Coulomb interactions are unscreened at long distance [25].

In the case of pristine C_3N, a nitrogen atom has an extra electron and shifts Dirac cone bands to the lower energy [15,16,23]. Most importantly, like graphene lattice, both inversion and time-reversal symmetries exist simultaneously in C_3N lattice when two N atoms are third-nearest neighbors. Therefore, C_3N has a Dirac cone, although an extra electron takes linear bands away from E_F. It motivates us to evaluate dielectric function and the effective Coulomb matrix elements in hexagonal C_3N from bulk to nanoribbons. The effective Coulomb interaction between localized electrons plays an important role in constructing a generic second-quantized Hamiltonian for C_3N and other carbon-nitrogen alloys and gives us useful information for describing the reason behind electronic and magnetic ordering.

The aim of the present paper is to introduce new materials with nonconventional screening and investigate the effects of reduced dimensionality and electronic band dispersion on electron screening. In this way we calculate the on-site and the long-range Coulomb interaction between p_z electrons in C_3N, hydrogenated C_3N, and C_3N nanoribbons by employing *ab initio* calculations in conjunction with the random-phase approximation (RPA) [35,36] within the full-potential linearized augmented plane wave (FLAPW) method [37]. Our results show that the electron screening in monolayer C_3N are weaker than the ones in pristine graphene due to its particular band dispersion. The considerable long-range Coulomb interactions in the monolayer of C_3N are even larger than the values for one-dimensional C_3NNRs systems with the larger band gap. Furthermore, a moderate screening of interactions in metallic bilayers shows that hexagonal C_3N materials are nonconventional from the point of view of electron-electron interaction and electron screening.

The rest of this paper is organized as follows: The computational methods, correlated subspace, and Wannier function's validity are discussed in detail in Sec. II, Section III deals with
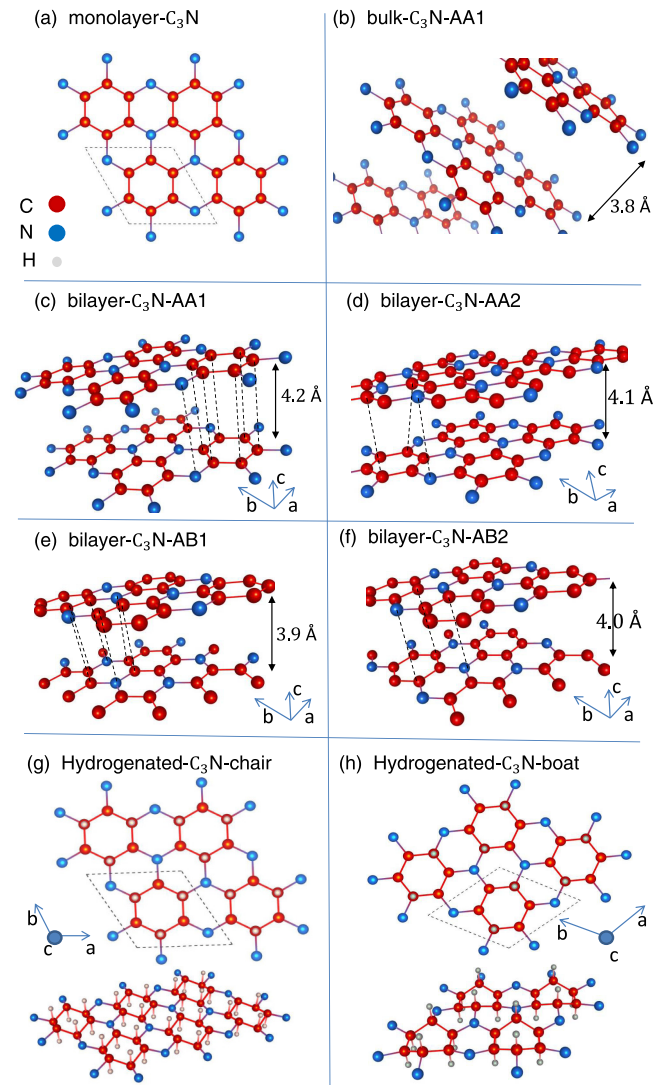

FIG. 1. Hexagonal crystal structures of (a) top view of C_3N monolayer, (b) C_3N 3D bulk, (c) bilayer C_3N-AA1, (d) bilayer C_3N-AA2, (e) bilayer C_3N-AB1, (f) bilayer C_3N-AB2, (g) top and side views of chairlike hydrogenated C_3N, and (h) top and side views of boatlike hydrogenated C_3N. The blue, red, and gray circles exhibit N, C, and H atoms, respectively.

the results and discussion, and finally, in Sec. IV we present the summary and outlook.

II. COMPUTATIONAL DETAILS

The top view crystal structure of pure monolayer of C_3N is presented in Fig. 1(a). The basic unit cell is hexagonal and contains six C atoms with two N atoms with a lattice constant of 4.88 Å. C_3N structure has time-reversal and D_{6h} point group symmetries. In the unit cell of C_3N, two N atoms are mutually transformed under C_6 rotation, similar to two nonequivalent sublattices in graphene and six C atoms form a benzene ring. Thus, two of energy bands of C_3N reproduces a Dirac cone [38,39]. As a result, the Dirac node is protected at energy-degenerate K and K' points in momentum space. In the Supplemental Material (SM) we provide discussion based
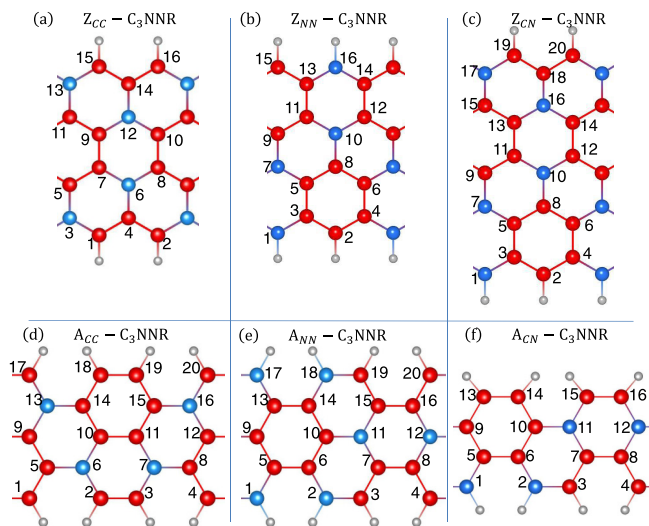
FIG. 2. Two types of edges for C_3N nanoribbons: Geometrical structures of different zigzag edges in the C_3NNRs (a) the pure C edges Z_{CC}-C_3NNR with ribbon width of 9.17 Å, (b) N atoms exist on both edges Z_{NN}-C_3NNR with ribbon width of 9.25 Å, (c) N atoms exist only in one edge Z_{CN}-C_3NNR with ribbon width of 11.31 Å. (d) A_{CC}-C_3NNR with ribbon width of 6.72 Å, (e) A_{NN}-C_3NNR with ribbon width of 6.70 Å, and (f) A_{CN}-C_3NNR with ribbon width of 5.48 Å are the same as (a), (b), and (c) for armchair C_3NNR.

on symmetry analysis to understand the nature of Dirac cone formation, degeneracy at high symmetry points, and approximate band structure for a C_3N lattice [40]. For the bilayer of C_3N there are four choices with the same lattice constant of 4.86 Å: (i) to place all the atoms in the first layer exactly on top of similar atoms in the second layer denoted by C_3N-AA1 with layer spacing of 4.20 Å [see Fig. 1(c)]. (ii) The same as C_3N-AA1 but the first layer is shifted by a half-lattice constant along the diagonal direction as in Fig. 1(d) and denoted by C_3N-AA2 with a layer spacing of 4.10 Å. (iii) and (iv) Taking the AA1 (AA2) structure and shifting one of the layers along the diagonal direction by 1/3 of the lattice constant which is denoted by C_3N-AB1 (C_3N-AB2) with a layer spacing of 3.94 (4.05) Å and presented in Fig. 1(e) [Fig. 1(f)]. Simulation of all considered 2D systems is based on the slab model having a 20 Å vacuum separating them. The crystal structure of bulk C_3N-AA1 is the same as a monolayer with a difference that the considered distance in the slab model is 3.84 Å [see Fig. 1(b)]. We also simulate the crystal structure of hydrogenated C_3N with two configurations, namely, chairlike and boatlike C_3N as shown in Figs. 1(g) and 1(h), respectively. To simulate a nanoribbon of C_3N we consider orthorhombic unit cells with two different shapes of nanoribbon edges, namely zigzag and armchair edges, as presented in Figs. 2(a)–2(c) and Figs. 2(d)–2(f), respectively. In the zigzag shape there are three choices: (a) only carbon atoms are placed along the ribbon edges and form a zigzag pattern Z_{CC}-C_3NNR with lattice constants of $a = 4.85$ Å and $b = 24.2$ Å. (b) Carbon and nitrogen atoms are placed along the ribbon edges in between Z_{NN}-C_3NNR with lattice constants of $a = 4.81$ Å and $b = 24.2$ Å. (c) Carbon atoms are placed along one of the ribbon edges, while both nitrogen and carbon atoms are placed

along another ribbon edge Z_{CN}-C_3NNR with lattice constants of $a = 4.84$ Å and $b = 26.3$ Å. As shown in Figs. 2(d)–2(f), a similar structure holds for the armchair edge, namely (d) A_{CC}-C_3NNR, (e) A_{NN}-C_3NNR, and (f) A_{CN}-C_3NNR with lattice constants of $a = 8.40$ Å and $b = 21.8$ Å. The edge carbon atoms are passivated by hydrogen atoms.

DFT calculation are carried out using Fluer code based on the full-potential linearized augmented plane-wave (FLAPW) [37] method within the GGA in the Perdew-Burke-Ernzerhof (PBE) parametrization [41] for the exchange-correlation energy functional. The SPEX code [42] uses DFT outputs to determine the strength of the partially screened (Hubbard U) and the fully screened (W) Coulomb interaction between correlated electrons from the first-principles cRPA and RPA methods, respectively [35,36,43]. $24{\times}1{\times}1$, $16{\times}16{\times}1$, and $8{\times}8{\times}8$ k-point grids are used for unit cells of 1D C_3N nanoribbons, 2D considered systems, and 3D bulk C_3N, respectively. The cutoff energy of $E_{cut} = 250$ and 350 Ry are chosen for the plane waves of 2D and 1D systems, respectively [40]. The maximally localized Wannier functions (MLWFs) are constructed with the Wannier90 library [44,45] using ten bands per carbon atom. In RPA calculations, a dense k-point grid we use for 1D, 2D, and 3D systems are $30{\times}1{\times}1$, $12{\times}12{\times}1$, and $6{\times}6{\times}6$, respectively. For each system, the Broyden-Fletcher-Goldfarb-Shanno quasi-Newton algorithm is used to relax the internal coordinates of the N and C atoms and possible distortions with convergence threshold on forces for ionic minimization as small as 10^{-4} eV/Å.

When performing calculations for layered materials, the weak van der Waals interaction should be considered in the structure optimization. So, we found the lattice parameters and atomic position of all atoms in crystal coordinates by incorporating van der Waals (vdW) interactions via the Grimme-D3 approach [46]. As reported in Table II of the SM [40], for C_3N-bulk and C_3N-AA1, we obtain that lattice parameters and the position of atoms are not too different from the results without interlayer interaction and it does not effect the Coulomb parameters by taking into account the dispersion interaction. The variation of U for C_3N-bulk and C_3N-AA1 amounts to about 0.1–0.3 eV, as a consequence, the value of Hubbard U interactions for two calculations are more or less the same.

To find correlated subspace and subsequently to verify the validity of Wannier function, first we calculate the projected band structure and orbital-resolved density of states (DOS) for all systems which will be discussed in detail in the next section. Here we have only plotted an orbital projected band structure of one candidate for each group, namely monolayer-C_3N, bulk C_3N, bilayer C_3N-AB1, hydrogenated C_3NH_3-boat, and Z_{NN}-C_3NNR in Fig. 3 that resolve the contribution of C and N atoms. As an example, the monolayer of C_3N shows well-isolated p_z bands in which the dominant contributions to the correlated states at the vicinity of Fermi energy comes from the p_z orbitals of the C atoms (conduction bands) and p_z orbitals of the N atoms (valence bands). This argument is more or less the same for bulk C_3N, bilayer, C_3N-AB1, and Z_{NN}-C_3NNR as presented in Figs. 3(b), 3(c), and 3(e), respectively. Plotting similar projected band representation, correlated subspaces can be obtained for all considered systems. Note that since p_z states are extended to
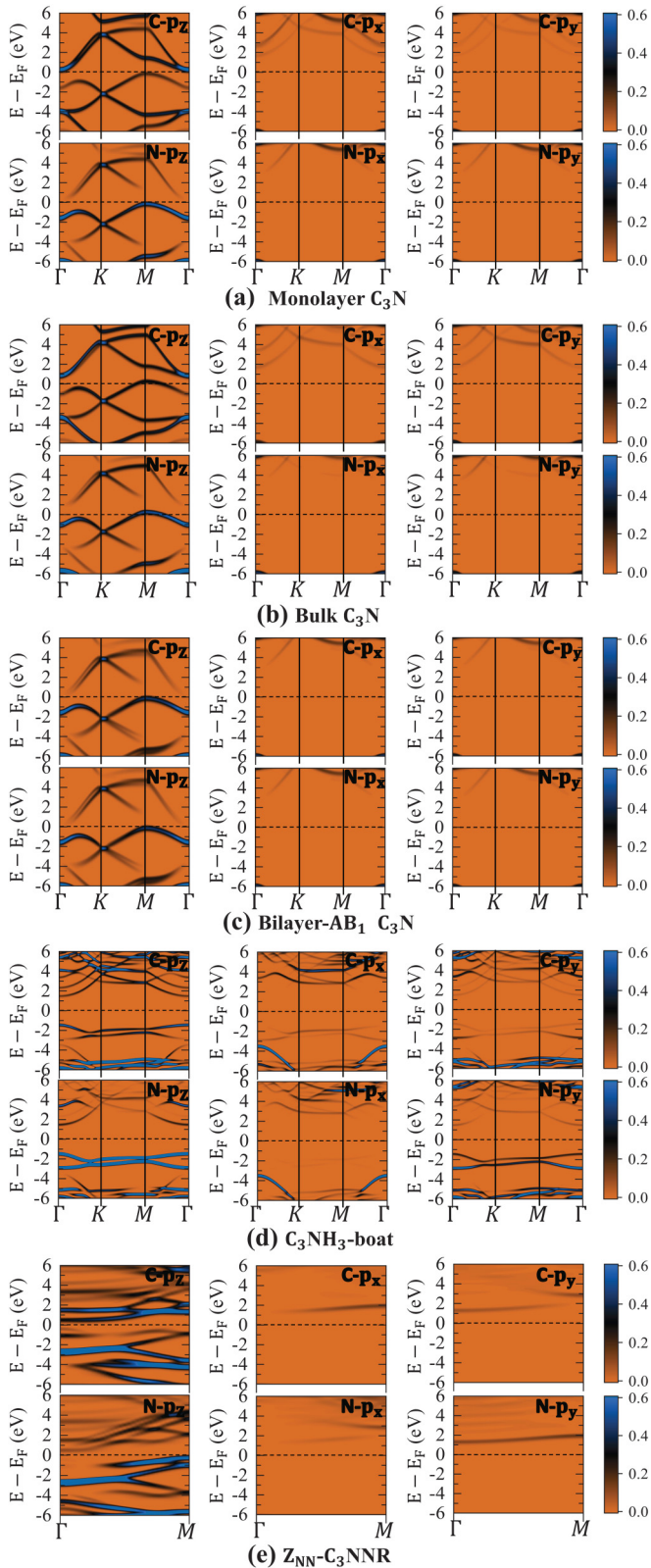
FIG. 3. Orbital-projected band structures for (a) monolayer C_3N, (b) bulk C_3N, (c) bilayer C_3N-AB1, (d) hydrogenated C_3NH_3-boat, and (e) Z_{NN}-C_3NNR. The results for p_z, p_x, and p_y are presented separately. The Fermi level is set to zero energy.
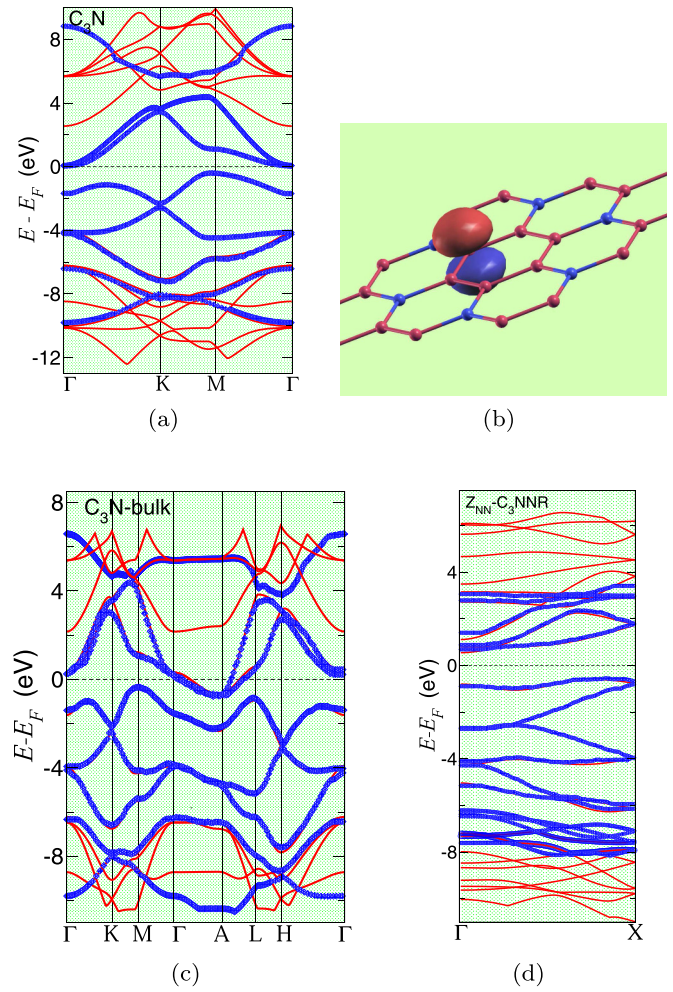

FIG. 4. (a) DFT-PBE (red) and Wannier interpolated band structures (blue) of C_3N monolayer. (b) The p_z-like MLWF for C atoms of C_3N. (c) and (d) The comparison of Wannier interpolation with DFT-PBE band structure for C_3N-bulk and Z_{NN}-C_3NNR.

very high energies, they overlap with s, p_x, and p_y bands in the region out of -6 to 6 eV. So, we have used a large number of bands for the construction of the Wannier orbitals to ensure that the entire correlated p_z electron property is included. In hydrogenated C_3N, namely chairlike and boatlike C_3N, our projected band [see also Fig. 5(p)] in Fig. 3(d) indicates that the p_z states of C or N atoms are not isolated from the p_x, p_y, and s states. It could, therefore, be necessary to extend the present p_z subspace by including the full s and p shell (sp^3) for hydrogenated C_3N.

To verify the adequacy of calculated Wannier functions, in Fig. 4 for C_3N-monolayer, C_3N-bulk, and Z_{NN}-C_3NNR, we compare the DFT-PBE band structure (red solid line) with the corresponding Wannier-interpolated bands (blue dots) obtained with p_z Wannier orbitals on the carbon and nitrogen sites. As seen from Fig. 4, the agreement between the original band and the Wannier interpolated band is almost good for the bands near Fermi level. But deviations appear for the bands
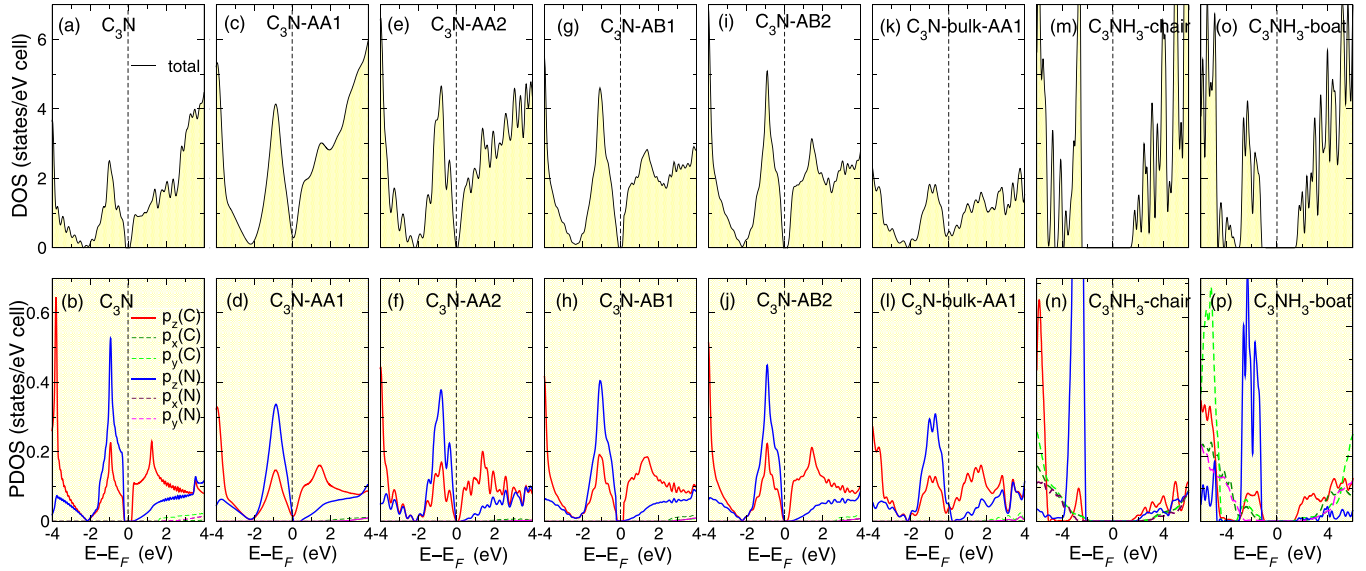
FIG. 5. Total and projected DOS: (a) and (b) monolayer C_3N, (c) to (j) various type of bilayer C_3N, (k) and (l) 3D bulk C_3N, and (m) to (p) hydrogenated C_3N.

far from Fermi energy E_F. It is expected due to the overlap of other states with p_z states when we move away from E_F. The wave function presented in Fig. 4(b) indeed looks like a p_z orbital.

In contrast to d materials, someone may encounter the problem to construct the Wannier bands for some of the systems like C_3N-bulk due to the presence of extended p states. For d materials, we only required a few states in the construction of the Wannier due to the disentanglement of d bands of atoms with others [29,30,47]. But, to converge it in the case of C_3N-bulk, we first picked out the orbital numbers from energy eigenvalues and then applying trial and error we found the best orbital number for constructing the Wannier function. In other words, it needs a large number of bands and trial and error for the construction of the Wannier orbitals to ensure that the entire correlated p_z electron property is included. Despite this attempt, we can see a signature of poor convergence in the Wannier spread minimization in the case of C_3N-bulk. Although the rattling of the Wannierized bands can be seen in the case of C_3N-bulk, it is not serious enough to worry about long-range hopping integrals.

In the following we briefly describe the RPA and cRPA methods. The fully screened Coulomb interaction W is related to the bare Coulomb interaction V by

$$W(\boldsymbol{r}, \boldsymbol{r}', \omega) = \int d\boldsymbol{r}'' \epsilon^{-1}(\boldsymbol{r}, \boldsymbol{r}'', \omega) V(\boldsymbol{r}'', \boldsymbol{r}'), \quad (1)$$

where $\epsilon(\boldsymbol{r}, \boldsymbol{r}'', \omega)$ is the dielectric function. In the RPA of the dynamically screened Coulomb interaction, the dielectric function is given by

$$\epsilon(\boldsymbol{r}, \boldsymbol{r}', \omega) = \delta(\boldsymbol{r} - \boldsymbol{r}') - \int d\boldsymbol{r}'' V(\boldsymbol{r}, \boldsymbol{r}'') P(\boldsymbol{r}'', \boldsymbol{r}', \omega), \quad (2)$$

where the electron polarizability $P(\boldsymbol{r}'', \boldsymbol{r}', \omega)$ is related to the single-particle DFT Kohn-Sham eigenfunctions $\varphi_m(\boldsymbol{r})$ and

eigenvalues ϵ_m.

$$P(\boldsymbol{r}, \boldsymbol{r}', \omega) = 2 \sum_m^{\text{occ}} \sum_{m'}^{\text{unocc}} \varphi_m(\boldsymbol{r}) \varphi_{m'}^*(\boldsymbol{r}) \varphi_m^*(\boldsymbol{r}') \varphi_{m'}(\boldsymbol{r}')$$

$$\times \left[\frac{1}{\omega - \Delta_{mm'} + i\eta} - \frac{1}{\omega + \Delta_{mm'} - i\eta} \right]. \quad (3)$$

Here $\Delta_{mm'} = \epsilon_{m'} - \epsilon_m$, and η is a positive infinitesimal.

In order to calculate the effective Coulomb interaction between electrons in the correlated subspace (also called the partially screened interaction U), we need to exclude the screening due to the correlated subspace, So, in cRPA method we separate the full polarization function of Eq. (3) into two parts:

$$P = P_d + P_r, \quad (4)$$

where P_d includes only the transitions ($m \to m'$) between the states of the correlated subspace and P_r is the remainder. Then, the frequency-dependent effective Coulomb interaction is given by the matrix equation

$$U(\omega) = [1 - V P_r(\omega)]^{-1} V. \quad (5)$$

P_r excludes the screening processes that take place within the subspace.

The effective Coulomb matrix within the selected subspace in the MLWF basis are given by

$$U_{\boldsymbol{R} n_1, n_3, n_2, n_4}(\omega) = \iint d\boldsymbol{r} d\boldsymbol{r}' w_{n_1 \boldsymbol{R}}^*(\boldsymbol{r}) w_{n_3 \boldsymbol{R}}(\boldsymbol{r})$$

$$\times U(\boldsymbol{r}, \boldsymbol{r}', \omega) w_{n_4 \boldsymbol{R}}^*(\boldsymbol{r}') w_{n_2 \boldsymbol{R}}(\boldsymbol{r}'), \quad (6)$$

where $w_{n\boldsymbol{R}}(\boldsymbol{r})$ is the MLWF at site $\boldsymbol{R}$ with orbital index n, and the effective Coulomb potential $U(\boldsymbol{r}, \boldsymbol{r}', \omega)$ is calculated within the cRPA as described above. We define the average Coulomb matrix elements U in the static limit ($\omega = 0$) as

TABLE I. On-site (U_{00}), nearest neighbor (U_{01}), next-nearest neighbor (U_{02}), and third-nearest neighbor (U_{03}) partially screened Coulomb interactions (cRPA) for graphene, monolayer C_3N, four types of bilayer C_3N, 3D bulk C_3N-AA1, and hydrogenated chairlike and boatlike C_3N. The fully W (RPA) and unscreened V Coulomb interactions parameters are also given.

	Graphene	C_3N-monolayer	C_3N-AA1	C_3N-AA2	C_3N-AB1	C_3N-AB2	C_3N-bulk	C_3NH_3-chair	C_3NH_3-boat
V_{00} (eV)	16.75	16.88	17.14	17.24	17.01	16.87	17.70	16.33	16.28
V_{01} (eV)	8.53	8.78	8.66	8.72	8.75	8.69	8.79	8.83	8.04
V_{02} (eV)	5.45	5.58	5.56	5.52	5.55	5.51	5.55	5.53	5.30
V_{03} (eV)	4.72	4.90	4.82	4.84	3.79	3.76	4.87	4.89	4.82
U_{00} (eV)	8.70	9.27	7.15	7.34	8.50	8.59	6.94	8.49	8.31
U_{01} (eV)	4.05	4.98	3.31	3.52	4.32	4.41	2.59	4.84	4.43
U_{02} (eV)	2.57	3.52	1.37	1.55	2.93	3.12	1.25	3.39	3.17
U_{03} (eV)	2.21	3.16	1.26	1.42	2.26	2.53	1.01	2.82	2.83
W_{00} (eV)	4.24	5.29	4.21	4.36	4.51	4.64	4.09	6.80	6.34
W_{01} (eV)	2.07	2.49	1.39	1.37	2.26	2.28	1.25	3.77	3.25
W_{02} (eV)	1.12	1.43	0.35	0.39	1.18	1.25	0.34	2.62	2.38
W_{03} (eV)	1.04	1.36	0.29	0.35	1.09	1.16	0.28	2.37	2.11

follows:

$$U = \frac{1}{L} \sum_m U_{mm;mm}, \qquad (7)$$

where L is the number of localized orbitals, i.e., one for p_z and four for sp^3 orbitals. Similar to the definition of U, we can also define the so-called fully screened interaction parameters W as well as unscreened (bare) V.

III. RESULTS AND DISCUSSION

A. Monolayer, bilayer, bulk, and hydrogenated C_3N

We start with the discussion of on-site Coulomb interaction parameters for carbon atoms of monolayer, bilayer (AA1, AA2, AB1, AB2), bulk C_3N, and C_3NH_3 (boatlike, chairlike). Bare V_{00}, partially U_{00} (cRPA), and fully W_{00} (RPA) Coulomb interaction parameters are presented in Table I. For comparison, the corresponding Coulomb interaction values for graphene are presented in the first column of Table I. The calculated U_{00} (W_{00}) values turn out to be 9.27 eV (5.29 eV) for monolayer C_3N. This shows that the screening is weak in C_3N and we obtain large U and W. These values are slightly larger than corresponding interaction values for graphene $U = 8.7$ eV ($W = 4.5$ eV). To see the contribution of different orbitals as well as different atoms in the screening, we present the orbital-resolved DOS for C and N atoms for all considered systems. As seen in Fig. 5(b), starting with the well known graphene band dispersion and shifting the Dirac cone to the lower energy, we find that the contribution of p_z states around E_F are similar to graphene with the difference that small band gap $E_g = 0.39$ eV is observed in the case of C_3N. This small band gap reduces the contribution of s, p_x, $p_y \rightarrow p_z$ (as well as $p_z \rightarrow p_z$) transition and explains why C atoms of C_3N exhibit larger $U_{00}(W_{00}) = 9.27$ eV(5.29 eV) compared to the $U_{00}(W_{00}) = 8.70$ eV(4.24 eV) of graphene. Note that only a small band gap in C_3N is not expected to be able to give such a large reduction in screening and subsequently produce significantly sizable U and W that it is even larger than graphene as a semimetal. How bands are dispersed, and the presence of the Dirac cone below E_F, strongly influences

U and W, which confirms that the nonconventional screening of the Coulomb interaction seen in graphene is also observed in C_3N.

To see the effects of interlayer chemical interactions in the screening, the Coulomb interaction parameters for C atoms of C_3N-AA1, C_3N-AA2, C_3N-AB1, C_3N-AB2, and C_3N-bulk-AA1 are given in the next five columns of Table I. Since the bands close to E_F are mostly derived from out-of-plane oriented p_z states, as presented in Figs. 5(d), 5(f), 5(h), and 5(j), interlayer chemical coupling have strong effects on the electronic structure of these systems. Note that, in the AA1 structure [see Fig. 1(b) or 1(c)], all the atoms in the top layer are located directly on top of similar atoms in the bottom layer. In the AA2 structure [see Fig. 1(d)], the situation is the same as AA1, but the N atoms are located on the top of C atoms. As presented in Figs. 5(c) and 5(e), adding a single layer to C_3N monolayer as AA1 and AA2 stackings removes the band gap, and yet, the relevant states at the vicinity of the Fermi level are the p_z orbitals atoms. For C_3N-AB1 and C_3N-AB2 stacking patterns since only half of the atoms are exactly aligned, interlayer chemical interactions are weaker compared to AA1 and AA2 systems, as a consequence, the band gap of the monolayer is preserved. AB1 and AB2 bilayers of C_3N are indeed semiconductors with band gaps of 0.11 and 0.21 eV as shown in Figs. 5(g) and 5(i), respectively. We obtain almost the same values of U (W) for metallic (AA1, AA2) and nonmetallic (AB1, AB2) stacking patterns, the formers being about 1 eV smaller due to the existence of the metallic states. Since in the cRPA level, contribution of the p_z states around E_F to the screening through $p_z \rightarrow p_z$ transitions is totally excluded from the polarization function, regardless of whether the system is metallic or insulating, Coulomb parameters do not show variation from system to system. In other words, the slightly smaller Coulomb interactions U(W) 7.15 eV (4.21 eV) and 7.34 eV (4.36 eV) in C_3N-AA1, and C_3N-AA2, respectively, compared to the corresponding parameters for C_3N-AB1 and C_3N-AB2 bilayers, 8.5 eV (4.51 eV) and 8.6 eV (4.64 eV) (see Table I) indicates that the interlayer chemical coupling have small effects on Coulomb interactions. Moreover, the presence of the band gap in C_3N, C_3N-AB1, and C_3N-AB2 bilayers and qualitative

behavior of the size of the band gap for different systems are in good agreement with the behavior of the recent measurement of band gap in experiment [17,20]. Although the magnitude of the DFT+PBE band gap is significantly smaller than the corresponding band in the experiment due to the reason that the DFT band structure underestimates the gap in semiconductors. Subsequently, the large Coulomb matrix elements for C_3N (we will also see in hydrogenated C_3N) are in agreement with significant many-body corrections to the band gaps, which are in the range of 1 eV in these materials [20,48]. For C_3N-bulk (only the AA1 structure is shown), interlayer coupling is tenacious, and the p_z valence bands strongly overlap with conduction bands. In 3D systems, the number of screening channels is larger compared to 2D systems and the reduction of U and W is much more pronounced.

In the following we will consider the situation in which all C atoms in the C_3N are saturated by H atoms. Here the purpose of absorbing H atoms is to study its effect in the screening and compare the results with the corresponding Coulomb interaction of fully hydrogenated graphene, the so-called graphane. We consider two different shapes of hydrogenated C_3N systems, namely, chairlike hydrogenated C_3N and boatlike hydrogenated C_3N, depending on the location of H atoms. Note that the dominant contributions to the DOS close to E_F do not only come from the p_z orbitals of C and N atoms. The insight from orbital-resolved DOS depicted in Figs. 5(a) and 5(p) is that all p_x, p_y, p_z, and s orbitals are of comparable importance and must be incorporated into the U and W calculation. So, it is meaningless to compare the Coulomb matrix elements results of hydrogenated C_3N with the corresponding results for pure C_3N obtained with p_z Wannier orbitals. But, one can compare the results with Coulomb parameters of graphane. Considering sp^3 correlated subspace for C_3NH_3-boat and C_3NH_3-chair, we obtain the on-site U_{00} (W_{00}) values of 8.31 eV (6.34 eV) and 8.49 eV (6.80 eV), respectively. The hydrogen absorption on C_3N atoms severely increases the band gap up to 4.0 eV (3.1 eV), as a result, the transitions from occupied to unoccupied states hardly happen, and we expect large value of Coulomb parameters for hydrogenated C_3N even larger than the corresponding values of pure C_3N (although their correlated states are different). The almost same value of U compared to the monolayer of C_3N is attributed to the reason that the disappearance of π states close to E_F does not significant influence U. Compared to graphane [8], the resolved DOS for hydrogenated C_3N indicates larger contributions of the p_z orbitals of the N atoms [blue peak in Figs. 5(n) and 5(p)] in the screening and subsequently gives the smaller value of U and in particular W.

So far we have only considered the local matrix elements of Coulomb interactions. The long-range Coulomb interactions lead to nontrivial renormalization of the Dirac quasiparticle characteristics and play an important role in determining the phase diagram of hexagonal carbon-based materials [25,49–51]. Previous *ab initio* studies revealed that pristine graphene as a semimetal could not screen the long-range Coulomb interaction conventionally, and a significant nonlocal part of U was obtained [25,26]. The nonlocal (long-range) Coulomb matrix elements, namely nearest neighbor U_{01} (W_{01}), next-nearest neighbor U_{02} (W_{02}), and third-nearest neighbor U_{03} (W_{03}), are also reported for all systems in Table I. Due to

the existence of the band gap and particular band dispersion in C_3N-monolayer, C_3N-AB1, C_3N-AB2, and hydrogenated C_3N, the Coulomb interactions, in particular W_{0n}, are weakly screened at long distances and we find sizable off-site matrix elements. On the other hand, the situation is different in the case of bulk C_3N due to a comparatively large number of screening channels. For example, in the monolayer of C_3N we obtain the U_{01} value of 4.98 eV, which is significantly larger than $U_{01} = 2.59$ eV for the C_3N-bulk system.

In other words, in contrast to C_3N-bulk, in 2D C_3N systems and, as we will see in some of the C_3NNR, the screening is nonlocal, as a consequence, in the Fourier space it is described by momentum dependent macroscopic dielectric function. This is consistent with the results of Cudazzo *et al.* that in 2D systems the macroscopic screening is q dependent showing a logarithmic divergence for small distances [52]. Experimentally, one of the consequences of such a nonconventional screening is the large exciton binding energy [55,56]. Moreover, for graphene, cRPA calculations give $\epsilon = 2.4$ for intermediate momentum q, and $\epsilon = 1$ for $q = 0$. This is fundamentally different for graphite $\epsilon = 2.5$ which is almost independent of the momentum q [25].

Interestingly, in metallic C_3N-AA1 and C_3N-AA2, off-site Coulomb interactions are still large and do not behave like ordinary metals, wherein the screening makes the interaction extremely short range. Similar arguments hold for the other off-site matrix elements, namely U_{02} and U_{03} in Table I. Note that not only long-range interaction for a monolayer of C_3N is the largest in our considered carbonitrides systems, but it is also almost 1 eV larger than the corresponding value of $U_{01} = 4.05$ eV for graphene [26]. This shows that graphene is not the only unique 2D system from the point of view of electron-electron interaction and electron screening.

B. C_3N nanoribbons

In this section we investigate whether and to what degree the Coulomb interactions would change if 2D C_3N turns to the nanoribbon (1D system) by cutting it in certain directions. We start with the discussion of the electronic structure for C_3N nanoribbons having six different edge configurations. For Z_{CC}-C_3NNR, Z_{CN}-C_3NNR, and A_{NN}-C_3NNR, our calculated total DOS and projected DOS in Fig. 6 reveals the existence of metallic states at the Fermi level, which is in good agreement with previous first-principles studies [23], while Z_{NN}-C_3NNR, A_{CC}-C_3NNR, and A_{CN}-C_3NNR are semiconductors with the band gap of 1.2, 0.7, and 1.3 eV, respectively, which reasonably agrees with the results of ultraviolet photoelectron spectroscopy [15,17]. In order to get insight into the contribution of different atoms to the total screening process, in the second row of Fig. 6 we present DOS for p_z orbitals of both C and N atoms. As pointed out, the relevant states at the vicinity of the Fermi level are p_z orbitals for all considered nanoribbons. So, we only show the DOS for p_z orbitals of each C and N atom.

In the first row of Fig. 7 we present bare interaction V, on-site effective Coulomb interaction parameters (Hubbard U), as well as the fully screened interaction W for p_z orbitals of all C and N atoms in the unit cell. To see the contribution of different C atoms in the screening, in the second row of
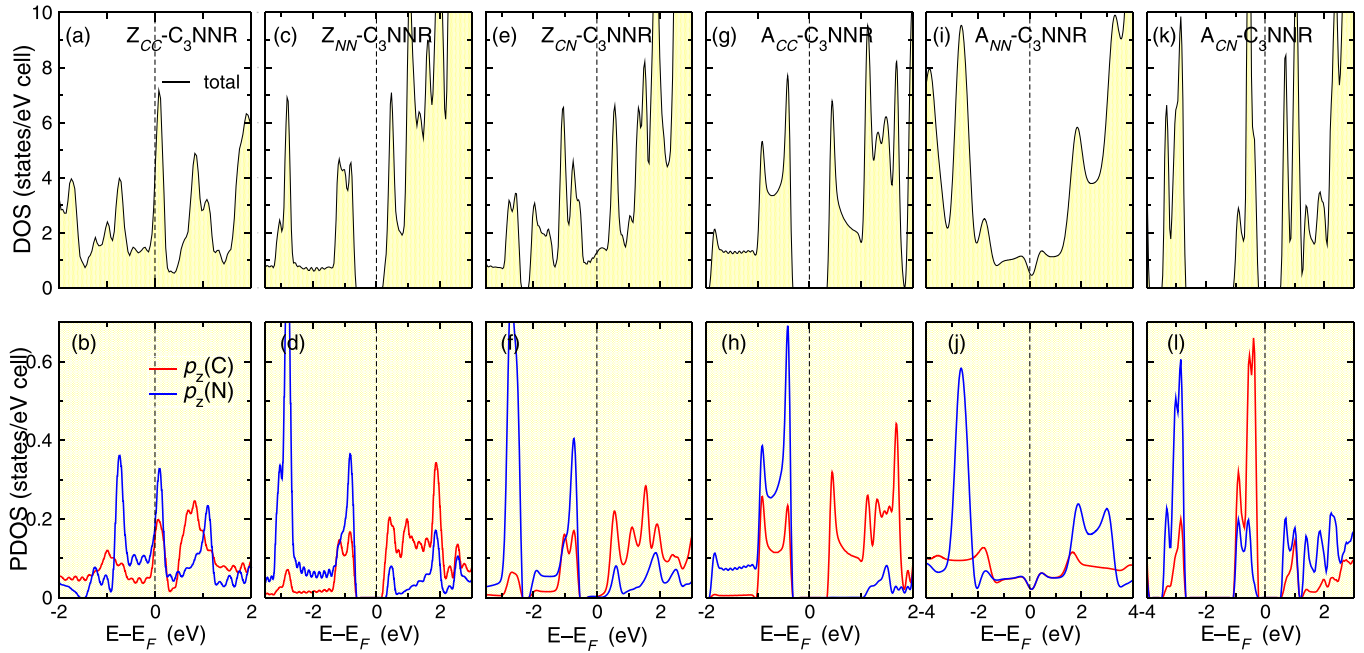
FIG. 6. Total and projected DOS: (a) and (b) Z_{CC}-C_3NNR, (c) and (d) Z_{NN}-C_3NNR, (e) and (f) Z_{CN}-C_3NNR, (g) and (h) A_{CC}-C_3NNR, (i) and (j) A_{NN}-C_3NNR, and (k) and (l) A_{CN}-C_3NNR.

Fig. 7, just below the Coulomb interaction of each system, we present the projected p_z DOS for one of the inner and edge C atoms. Conventions for labeling of atoms in the unit cell are given in Fig. 2. For comparison, the results for 2D C_3N are also presented in Fig. 7 with the dashed line.

The Coulomb parameters show strong variations from atom to atom in metallic systems. As an example, U (W) in Z_{CC}-C_3NNR varies between 2.0 eV (1.8 eV) and 7.0 eV (5.0 eV). These variations originate in the site dependence of the bare Coulomb interaction or the difference in the spread of
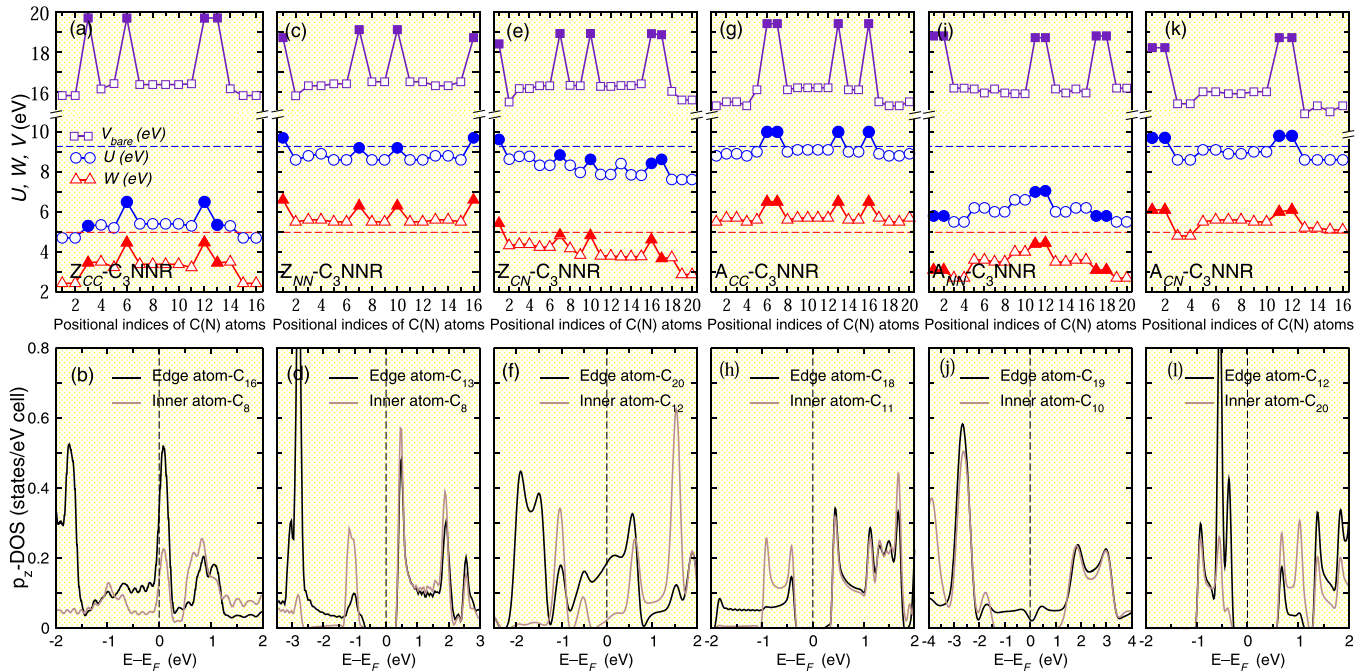

FIG. 7. Partially (fully) screened on-site interaction U (W) for p_z electrons of C (solid circles and triangles) and N (hollow circles and triangles) atoms, and projected DOS for inner and edge C atoms: (a) and (b) Z_{CC}-C_3NNR, (c) and (d) Z_{NN}-C_3NNR, (e) and (f) Z_{CN}-C_3NNR, (g) and (h) A_{CC}-C_3NNR, (i) and (j) A_{NN}-C_3NNR, and (k) and (l) A_{CN}-C_3NNR. For comparison, U and W of monolayer C_3N are also included (dashed lines). Horizontal ticks of upper rows are for position indices of C and N atoms in the nanoribbon unit cells which are shown in Fig. 2.

Wannier functions. On the other hand, the situation is different in the case of semiconducting systems, so that the interaction parameters for all C or N atoms are almost the same. The small value of fully screened interaction (RPA level) stem from sizable contribution of p_z states of the corresponding atoms at E_F. As seen in Fig. 7(b), C_{16} that is located at the edge has a large p_z peak around E_F, which indeed is responsible for the strong reduction in W. While the contribution of p_z states of C_8 around E_F is smaller and W turns out to be rather sizable yet. A similar argument more or less holds for other metallic nanoribbons and explains why C or N atoms at the edge exhibit small W values. In semiconductors, disappearance of the p_z states at the E_F reduces the screening through $p_z \rightarrow p_z$ as well as s, p_x, $p_y \rightarrow p_z$ transitions, thereby giving remarkably larger matrix elements compared to metallic systems.

In the following we discuss the screening of the long-range Coulomb interaction between p_z electrons in C_3NNR with armchair and zigzag edges. In Fig. 8(a), the nonlocal partially (fully) screened Coulomb interaction parameters along $U_\parallel$ and $W_\parallel$ and across the ribbon $U_\perp$ and $W_\perp$ are presented for all considered nanoribbons as a function of distance r between two C atoms. In Figs. 8(b) and 8(c) we have indicated atomic paths with a green (yellow) arrow where the long-range interactions along (across) the ribbons are calculated. For the nonmetallic systems, due to reduced dimensionality and the existence of the band gap, we find stronger off-site interactions compared to Coulomb parameters for metallic systems. U and W at short distances are sizable and decay slowly due to the weak screening. As an example of how large the long-range Coulomb interactions on the nonmetallic C_3NNRs are, consider the simplest C_2 and its first neighbor site C_3 along the A_{CC}-C_3NNR in Fig. 2(d). We find the fully nonlocal Coulomb interaction is 1.9 eV which is almost 0.6 eV smaller than $W_{01} = 2.49$ eV reported in Table I for the C_3N monolayer. Similar arguments hold for nonlocal interactions between second and third neighbors. Furthermore, the nonlocal Coulomb interaction across the ribbon is more or less the same as the one along the ribbon. Interestingly, despite that semiconducting C_3NNRs are in the lower dimension and have a bigger band gap compared to the monolayer of C_3N, their Hubbard U values and long-range interactions of p_z electrons are smaller. This means that similar to graphene, screening in pure 2D C_3N is also controversial. In graphene, nonconventional screening of Coulomb interaction stems from linearly dispersing bands. In C_3N, although N atoms open a band gap, the massless Dirac dispersion has to be preserved for symmetry reasons, and it only shifts Dirac cone bands to the lower energy.

Let us finalize the discussion by comparing the values of nonlocal bare interaction V and the corresponding nonlocal fully screened interaction W. For this purpose, in Fig. 8(a) we present the long-range bare interaction V by the solid purple line. Let us focus on the A_{CC}-C_3NNR as semiconducting nanoribbons. The difference $V - W$ is large at short distances, which decreases with increasing distance, and at long distance, it becomes zero. So, similar to the 2D systems, dielectric functions of semiconducting C_3NNRs are strongly dependent on q. This feature has a great impact on the optical and transport properties of them.

The situation is quite different in the case of metallic systems, namely Z_{CC}-C_3NNR, Z_{CN}-C_3NNR, and A_{NN}-C_3NNR

(a)

$Z_{NN} - C_3$NNR

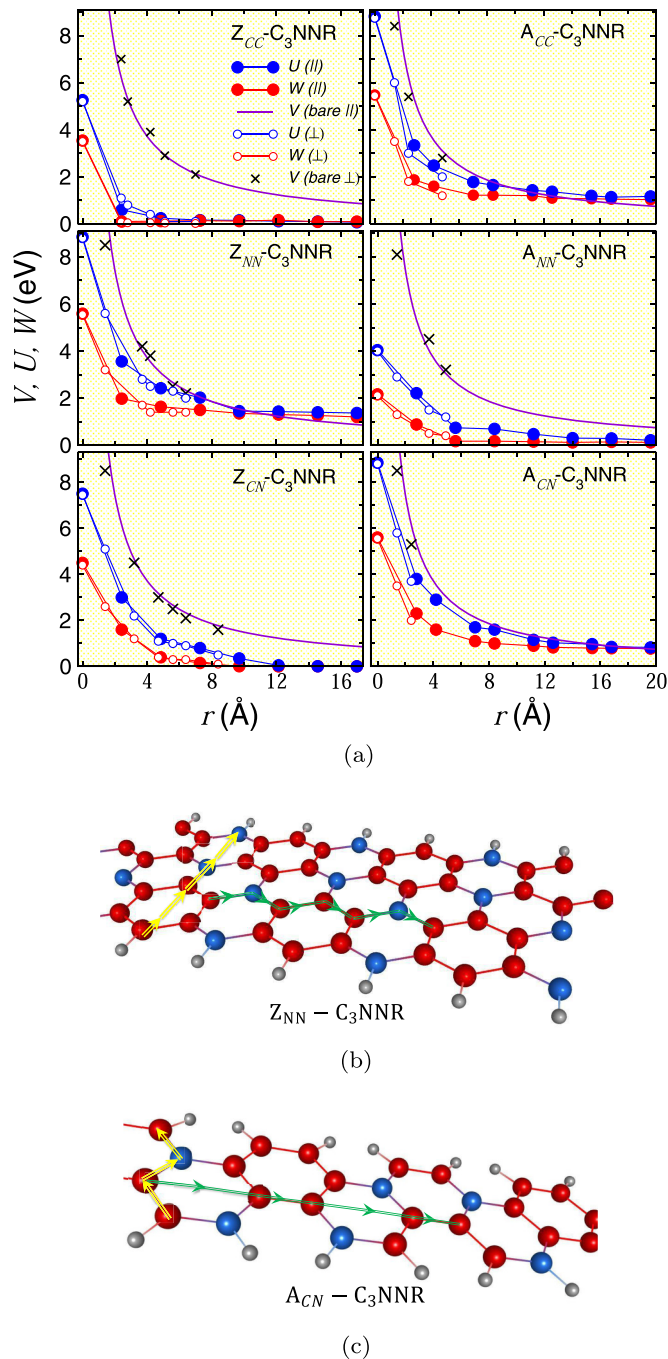(b)

$A_{CN} - C_3$NNR

(c)

FIG. 8. (a) Partially (fully) screened Coulomb interaction $U(W)$ for C p_z electrons as a function of distance r for six considered C_3NNRs. Here the symbols ($\parallel$) and ($\perp$) correspond to interactions along with the ribbon and across the ribbon, which are shown with green and yellow lines in (b) and (c), respectively. For comparison, the unscreened interaction V is also presented. (b) and (c) Atomic paths where the long-range interactions are calculated for zigzag and armchair C_3NNRs, respectively. Green (yellow) path for along (across) the ribbon.

so that the U along the ribbon is fully screened at distances larger than 5, 12, and 14 Å, respectively, which are indicated in Fig. 8(a). For example in Z_{CC}-C_3NNR, the presence of sharp peak at E_F (most contribution belongs to the edge
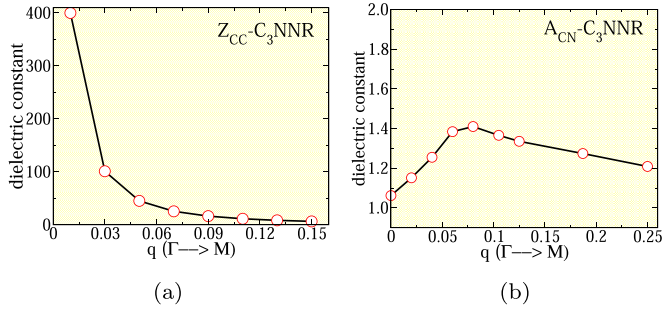
FIG. 9. Static dielectric function versus momentum q for two considered nanoribbons (a) metallic Z_{CC}-C_3NNR and (b) semiconducting A_{CN}-C_3NNR.

states) strongly affects the long-range interaction, making it completely short range. The large gradient of the Coulomb interaction in Z_{CC}-C_3NNR makes local and semilocal approximations to the exchange-correlation potential inconvenient [52–54].

Furthermore, we discuss the behavior of static dielectric function versus momentum q for two considered nanoribbons. The results are presented in Fig. 9(a) for metallic Z_{CC}-C_3NNR and Fig. 9(b) for semiconducting A_{CN}-C_3NNR. In Z_{CC}-C_3NNR, the screening caused by the presence of mobile charge carriers is strong and we obtain large ϵ values larger than 300 at $q \to 0$. The dielectric function ϵ can also be derived from bare interaction $V(r)$ divided by screened interaction $W(r)$. In metallic systems like Z_{CC}-C_3NNR, $W(r)$ drops sharply and become zero at short distances, as a consequence, the macroscopic dielectric constant gives a large value. This is consistent with Fig. S5(a) of the SM [40], in which we obtain large ϵ values of about 120 at large distances for Z_{CN}-C_3NNR, Z_{CC}-C_3NNR, and A_{NN}-C_3NNR.

In semiconducting nanoribbon A_{CN}-C_3NNR, dielectric constant at long wavelengths $\epsilon(q \to 0) \to 1$ indicates that interactions are unscreened at large distances. In fact, the difference $V - W$ decreases with increasing distance, and at large distances, the screened interaction has to approach $1/\epsilon r$. Since long-wavelength behavior of $\epsilon(q)$ determines the screening of the long-range tails of the Coulomb interaction, we describe screening of long-range region by $V(r)/W(r) \to 1$ for $r \to \infty$ (see Fig. S5(b) of the SM [40]). This can be observed from the data in Fig. 8, where $V - W$ difference is very close to zero for nonmetallic nanoribbons.

IV. SUMMARY AND OUTLOOK

We have determined the strength of the local and long-range effective Coulomb interaction $U(W)$ in honeycomb C_3N from bulk to nanoribbons by employing the parameter-free cRPA(RPA) method. The calculated $U(W)$ parameters in the C_3N monolayer are larger than the ones in pristine graphene due to its special band dispersion. In the bilayer of C_3N, since the bands close to E_F are mostly derived from out-of-plane oriented p_z states, Coulomb parameters weakly depend on stacking patterns and interlayer chemical interaction have a small effect in the electron screening. Furthermore, we discuss the screening of the long-range Coulomb interaction between p_z electrons in C_3NNR with armchair and zigzag edges. Despite that nonmetallic C_3NNRs are one-dimensional systems and have a bigger band gap compared to the monolayer of C_3N, their Hubbard U values are almost the same and long-range interactions are only 1 eV larger. Strong long-range Coulomb interactions in monolayer of C_3N and moderate screening of interaction in metallic bilayers shows that graphene is not the only unique system from the point of view of electron-electron interaction. The presence of linear band dispersion below E_F in C_3N has a strong influence on electron screening and confirms that the nonconventional screening of the Coulomb interaction seen in graphene is also observed in C_3N.

One of the consequences of such nonconventional screening or sizable long-range Coulomb interactions which are seen in the C_3N compounds is the formation of exciton with large binding energy. Other 1D and 2D semiconductors such as armchair GNRs [55,56], hexagonal boron nitride [57–59], graphane [52], fluorographene [60], and transition-metal dichalcogenides [61–64] possess tightly bound excitons, and their dispersion strongly deviates from the hydrogenic Rydberg series, indicating a significantly nonlocal dielectric screening of the Coulomb interaction in these materials. This effect has not been studied in C_3N compounds yet. Another important point is the presence of edge states in metallic nanoribbons such as Z_{CC}-C_3NNR [see Fig. 7(b)] which give rise to a relatively large contribution to the DOS at E_F and thus Coulomb interaction around $U = 4.9$ eV makes the system unstable to formation of ferromagnetic order because the Stoner criterion $UD(E_F) > 1$ is satisfied. The study of magnetic ordering and more detailed analyses in metallic systems are beyond the scope of this paper and can be considered for future studies. These obtained Coulomb interaction parameters are important not only for a basic understanding of the physics of carbon nitrogen alloy but also for use in a physically motivated model which paves the path for many other studies describing electronic, magnetic, and optical properties of these materials.

[1] A. K. Geim and K. S. Novoselov, Nat. Mater. **6**, 183 (2007).

[2] M. I. Katsnelson, Mater. Today **10**, 20 (2007).

[3] P. Vogt, P. De Padova, C. Quaresima, J. Avila, E. Frantzeskakis, M. C. Asensio, A. Resta, B. Ealet, and G. Le Lay, Phys. Rev. Lett. **108**, 155501 (2012).

[4] E. Bianco, S. Butler, S. Jiang, O. D. Restrepo, W. Windl, and J. E. Goldberger, ACS Nano **7**, 4414 (2013).

[5] F. Zhu, W. Chen, Y. Xu, C. Gao, D. Guan, C. Liu, D. Qian, S. C. Zhang, and J. Jia, Nat. Mater. **14**, 1020 (2015).

[6] J. O. Sofo, A. S. Chaudhari, and G. D. Barber, Phys. Rev. B **75**, 153401 (2007).

[7] D. C. Elias, R. R. Nair, T. M. G. Mohiuddin, S. V. Morozov, P. Blake, M. P. Halsall, A. C. Ferrari, D. W. Boukhvalov, M. I. Katsnelson, A. K. Geim, and K. S. Novoselov, Science **323**, 610 (2009).

[8] E. Şaşıoğlu, H. Hadipour, C. Friedrich, S. Blugel, and I. Mertig, Phys. Rev. B **95**, 060408(R) (2017).

[9] H. Hadipour, Phys. Rev. B **99**, 075102 (2019).

[10] X. Li, X. Wang, L. Zhang, S. Lee, and H. Dai, Science **319**, 1229 (2008).

[11] C. L. Kane and E. J. Mele, Phys. Rev. Lett. **95**, 146802 (2005).

[12] Y. Zhang, Y. W. Tan, H. L. Stormer, and P. Kim, Nature (London) **438**, 201 (2005).

[13] Y. Yekta, H. Hadipour, and S. A. Jafari, arXiv:2108.08183.

[14] M. I. Katsnelson, K. S. Novoselov, and A. K. Geim, Nat. Phys. **2**, 620 (2006).

[15] S. Yang, W. Li, C. Ye, G. Wang, H. Tian, C. Zhu, P. He, G. Ding, X. Xie, Y. Liu, Y. Lifshitz, S. Lee, Z. Kang, and M. Jiang, Adv. Mater. **29**, 1605625 (2017).

[16] H. J. Xiang, B. Huang, Z. Y. Li, S. H. Wei, J. L. Yang, and X. G. Gong, Phys. Rev. X **2**, 011003 (2012).

[17] J. Mahmood, E. K. Lee, M. Jung, D. Shin, H.-J. Choi, J.-M. Seo, S.-M. Jung, D. Kim, F. Li, M. Soo Lah, N. Park, H.-J. Shin, J. H. Oh, and J.-B. Baek, Proc. Natl. Acad. Sci. USA **113**, 7414 (2016).

[18] J. Xu, J. Mahmood, Y. Dou, S. Dou, F. Li, L. Dai, and J.-B. Baek, Adv. Mater. **29**, 1702007 (2017).

[19] A. K. Mandal, J. Mahmood, and J.-B. Baek, ChemNanoMat **3**, 373 (2017).

[20] W. Wei, S. Yang, G. Wang, T. Zhang, W. Pan, Z. Cai, Y. Yang, L. Zheng, P. He, L. Wang, A. Baktash, Q. Zhang, L. Liu, Y. Wang, G. Ding, Z. Kang, B. I. Yakobson, D. J. Searles, and Q. Yuan, Nat. Electron. **4**, 486 (2021).

[21] S. Kumar, S. Sharma, V. Babar, and U. Schwingenschlogl, J. Mater. Chem. A **5**, 20407 (2017).

[22] B. Mortazavi, Carbon **118**, 25 (2017).

[23] M. B. Tagani and S. Izadi, J. Appl. Phys. **124**, 084304 (2018).

[24] D. Wang, Y. Bao, T. Wu, S. Gan, D. Han, and L. Niu, Carbon **134**, 22 (2018).

[25] T. O. Wehling, E. Sasioglu, C. Friedrich, A. I. Lichtenstein, M. I. Katsnelson, and S. Blugel, Phys. Rev. Lett. **106**, 236805 (2011).

[26] H. Hadipour, E. Şaşıoğlu, F. Bagherpour, C. Friedrich, S. Blugel, and I. Mertig, Phys. Rev. B **98**, 205123 (2018).

[27] W. Yu, J. Li, T. Seng Herng, Z. Wang, X. Zhao, X. Chi, W. Fu, I. Abdelwahab, J. Zhou, J. Dan, Zh. Chen, Zhi Chen, Z. Li, J. Lu, S. J. Pennycook, Y. Ping Feng, J. Ding, and K. Ping Loh, Adv. Mater. **31**, 1903779 (2019).

[28] B. Huang, G. Clark, E. Navarro-Moratalla, D. R. Klein, R. Cheng, K. L. Seyler, D. Zhong, E. Schmidgall, M. A. McGuire, D. H. Cobden, W. Yao, Di Xiao, P. Jarillo-Herrero, and X. Xu, Nature (London) **546**, 270 (2017).

[29] Y. Yekta, H. Hadipour, E. Şaşıoğlu, C. Friedrich, S. A. Jafari, S. Blugel, and I. Mertig, Phys. Rev. Materials **5**, 034001 (2021).

[30] A. Karbalaee Aghaee, S. Belbasi, and H. Hadipour, Phys. Rev. B **105**, 115115 (2022).

[31] M. Naguib, V. N. Mochalin, M. W. Barsoum, and Y. Gogotsi, Adv. Mater. **26**, 992 (2014).

[32] H. Hadipour and Y. Yekta, Phys. Rev. B **100**, 195118 (2019).

[33] E. H. Hwang and S. Das Sarma, Phys. Rev. B **75**, 205418 (2007).

[34] T. Ando, A. B. Fowler, and F. Stern, Rev. Mod. Phys. **54**, 437 (1982).

[35] F. Aryasetiawan, M. Imada, A. Georges, G. Kotliar, S. Biermann, and A. I. Lichtenstein, Phys. Rev. B **70**, 195104 (2004); F. Aryasetiawan, K. Karlsson, O. Jepsen, and U. Schonberger, *ibid.* **74**, 125106 (2006); T. Miyake, F. Aryasetiawan, and M. Imada, *ibid.* **80**, 155134 (2009).

[36] E. Şaşıoğlu, C. Friedrich, and S. Blugel, Phys. Rev. B **83**, 121101(R) (2011); Phys. Rev. Lett. **109**, 146401 (2012).

[37] See http://www.flapw.de.

[38] T. Kameda, F. Liu, S. Dutta, and K. Wakabayashi, Phys. Rev. B **99**, 075426 (2019).

[39] F. Liu, M. Yamamoto, and K. Wakabayashi, J. Phys. Soc. Jpn. **86**, 123707 (2017).

[40] See Supplemental Material at http://link.aps.org/supplemental/10.1103/PhysRevMaterials.6.094004 for details of symmetry analysis, convergence parameters, effect of dispersion interaction, and the behavior of static dielectric function, which includes Refs. [25,46,52].

[41] J. P. Perdew, K. Burke, and M. Ernzerhof, Phys. Rev. Lett. **77**, 3865 (1996).

[42] C. Friedrich, S. Blugel, and A. Schindlmayr, Phys. Rev. B **81**, 125102 (2010).

[43] Y. Nomura, M. Kaltak, K. Nakamura, C. Taranto, S. Sakai, A. Toschi, R. Arita, K. Held, G. Kresse, and M. Imada, Phys. Rev. B **86**, 085117 (2012); B.-C. Shih, Y. Zhang, W. Zhang, and P. Zhang, *ibid.* **85**, 045132 (2012).

[44] A. A. Mostofi, J. R. Yates, Y.-S. Lee, I. Souza, D. Vanderbilt, and N. Marzari, Comput. Phys. Commun. **178**, 685 (2008).

[45] F. Freimuth, Y. Mokrousov, D. Wortmann, S. Heinze, and S. Blugel, Phys. Rev. B **78**, 035120 (2008).

[46] J. Klimeš and A. Michaelides, J. Chem. Phys. **137**, 120901 (2012).

[47] A. Neroni, E. Şaşıoğlu, H. Hadipour, C. Friedrich, S. Blugel, I. Mertig, and M. Lezaic, Phys. Rev. B **100**, 115113 (2019).

[48] Y. Wu, W. Xia, W. Gao, F. Jia, P. Zhang, and W. Ren, 2D Mater. **6**, 015018 (2019).

[49] I. F. Herbut, Phys. Rev. Lett. **97**, 146401 (2006).

[50] C. Honerkamp, Phys. Rev. Lett. **100**, 146404 (2008).

[51] V. N. Kotov, B. Uchoa, V. M. Pereira, F. Guinea, and A. H. Castro Neto, Rev. Mod. Phys. **84**, 1067 (2012).

[52] P. Cudazzo, I. V. Tokatly, and A. Rubio, Phys. Rev. B **84**, 085406 (2011).

[53] J. Deslippe, M. Dipoppa, D. Prendergast, M. V. O. Moutinho, R. B. Capaz, and S. G. Louie, Nano Lett. **9**, 1330 (2009).

[54] M. van Schilfgaarde and M. I. Katsnelson, Phys. Rev. B **83**, 081409(R) (2011).

[55] R. Denk, M. Hohage, P. Zeppenfeld, J. Cai, C. A. Pignedoli, H. Sode, R. Fasel, X. Feng, K. Mullen, S. Wang, D. Prezzi, A. Ferretti, A. Ruini, E. Molinari, and P. Ruffieux, Nat. Commun. **5**, 4253 (2014).

[56] G. Soavi, S. D. Conte, C. Manzoni, D. Viola, A. Narita, Y. Hu, X. Feng, U. Hohenester, E. Molinari, D. Prezzi, K. Mullen, and G. Cerullo, Nat. Commun. **7**, 11010 (2016).

[57] K. Watanabe, T. Taniguchi, and H. Kanda, Nat. Mater. **3**, 404 (2004).

[58] A. Montaghemi, H. Hadipour, F. Bagherpour, A. Yazdani, and S. Mahdavifar, Phys. Rev. B **101**, 075427 (2020).

[59] B. Arnaud, S. Lebègue, P. Rabiller, and M. Alouani, Phys. Rev. Lett. **96**, 026402 (2006).

[60] F. Karlicky and M. Otyepka, J. Chem. Theory Comput. **9**, 4155 (2013).

[61] A. Chernikov, T. C. Berkelbach, H. M. Hill, A. Rigosi, Y. Li, B. Aslan, D. R. Reichman, M. S. Hybertsen, and T. F. Heinz, Phys. Rev. Lett. **113**, 076802 (2014).

[62] K. He, N. Kumar, L. Zhao, Z. Wang, K. F. Mak, H. Zhao, and J. Shan, Phys. Rev. Lett. **113**, 026803 (2014).

[63] M. M. Ugeda, A. J. Bradley, S.-F. Shi, F. H. da Jornada, Y. Zhang, D. Y. Qiu, W. Ruan, S.-K. Mo, Z. Hussain, Z.-X. Shen, F. Wang, S. G. Louie, and M. F. Crommie, Nat. Mater. **13**, 1091 (2014).

[64] D. Y. Qiu, F. H. da Jornada, and S. G. Louie, Phys. Rev. Lett. **111**, 216805 (2013).